ACS APPLIED MATERIALS & INTERFACES

Research Article

www.acsami.org

Electrical Contacts in Monolayer Arsenene Devices

Yangyang Wang,*[,†,#] Meng Ye,[‡,#] Mouyi Weng,[∥] Jingzhen Li,[‡] Xiuying Zhang,[‡] Han Zhang,[‡] Ying Guo,[‡,⊥] Yuanyuan Pan,[‡] Lin Xiao,[†] Junku Liu,[†] Feng Pan,*[,∥] and Jing Lu*[,‡,§]

[†]Nanophotonics and Optoelectronics Research Center, Qian Xuesen Laboratory of Space Technology, China Academy of Space Technology, Beijing 100094, P. R. China

[‡]State Key Laboratory for Mesoscopic Physics and Department of Physics, Peking University, Beijing 100871, P. R. China

[§]Collaborative Innovation Center of Quantum Matter, Beijing 100871, P. R. China

[∥]School of Advanced Materials, Peking University Shenzhen Graduate School, Shenzhen 518055, P. R. China

[⊥]School of Physics and Telecommunication Engineering, Shaanxi University of Technology, Hanzhong 723001, P. R. China

Supporting Information

ABSTRACT: Arsenene, arsenic analogue of graphene, as an emerging member of two-dimensional semiconductors (2DSCs), is quite promising in next-generation electronic and optoelectronic applications. The metal electrical contacts play a vital role in the charge transport and photoresponse processes of nanoscale 2DSC devices and even can mask the intrinsic properties of 2DSCs. Here, we present a first comprehensive study of the electrical contact properties of monolayer (ML) arsenene with different electrodes by using *ab initio* electronic calculations and quantum transport simulations. Schottky barrier is always formed with bulk metal contacts owing to the Fermi level pinning (pinning factor S = 0.33), with electron Schottky barrier height (SBH) of 0.12, 0.21, 0.25, 0.35, and 0.50 eV for Sc, Ti, Ag, Cu, and Au contacts and hole SBH of 0.75 and 0.78 eV for Pd and Pt contacts, respectively. However, by contact with 2D graphene, the Fermi level pinning effect can be reduced due to the suppression of metal-induced gap states. Remarkably, a barrier free hole injection is realized in ML arsenene device with graphene-Pt hybrid electrode, suggestive of a high device performance in such a ML arsenene device. Our study provides a theoretical foundation for the selection of favorable electrodes in future ML arsenene devices.

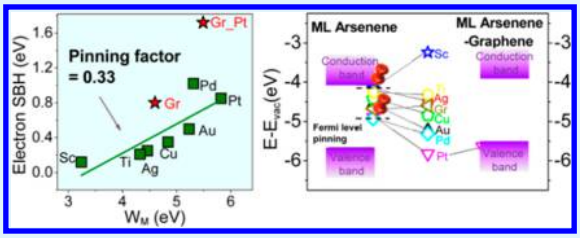

KEYWORDS: *monolayer arsenene, electrical contact, Schottky barrier, Fermi level pinning, first-principles calculation*

INTRODUCTION

Two dimensional semiconductors (2DSCs) are competitive alternates of conventional semiconductors for further generation of electronic and optoelectronic devices. Owing to the ultrathin geometry and dangling-bond-free interface, 2DSCs often exhibit high electrostatic gating efficiency and fewer trap states at the surface, and thereby have reduced short channel effect, which renders them extremely promising to extend Moore's law down to sub-10 nm scales. Hexagonal monolayer (ML) arsenene and antimonene, the group VA analogues of graphene, have attracted interest recently as new members of 2DSCs,[1−14] especially in light of the successful experimental synthesis of multilayer arsenene nanoribbons,[15] multilayer antimonene,[16−22] and antimonene nanoribbons.[23] ML arsenene is predicted to have a quasiparticle and optical band gap of 2.47 and 1.6 eV, respectively, in terms of GW and Bethe-Salpeter equation calculations,[4] which can be measured from the photoemission and inverse photoemission/scanning tunneling spectroscopy/photoluminescence spectroscopy and photoluminescence spectroscopy, respectively. The two band gaps are larger than the respective values of ML black phosphorene (2.47 vs 2.0−2.2 eV and 1.6 vs 1.3 eV).[24,25] The band gap in ML arsenene is also subject to a modulation by strain, electric field, or defect engineering.[2,5−9] Therefore, ML arsenene is quite promising in electronics and optoelectronics applications. According to *ab initio* quantum transport simulations, sub-10 nm ML arsenene metal-oxide-semiconductor field effect transistors (MOSFETs) can satisfy both the high performance and low power requirements of the International Technology Roadmap for Semiconductors (ITRS) in the next decade.[3,4] ML arsenene MOSFETs outperform MoS_2 FETs with Ti electrodes and are comparable to black phosphorene and antimonene MOSFETs in terms of the on-current based on *ab initio* quantum transport simulations (Table S1).

However, the conventional doping strategy is not applicable to 2D devices, and metal electrode is often used to directly contact the 2DSC materials to inject carriers. Schottky barrier (SB) is usually formed at the 2DSC-metal electrode junctions owing to the Fermi level (E_f) pinning effect and plays a substantial role in the charge transport and photoresponse processes of 2DSC devices. The corresponding transistor is referred to as SB transistor. The SB impedes the carrier

Received: June 13, 2017
Accepted: August 7, 2017
Published: August 7, 2017

DOI: 10.1021/acsami.7b08513
ACS Appl. Mater. Interfaces XXXX, XXX, XXX−XXX

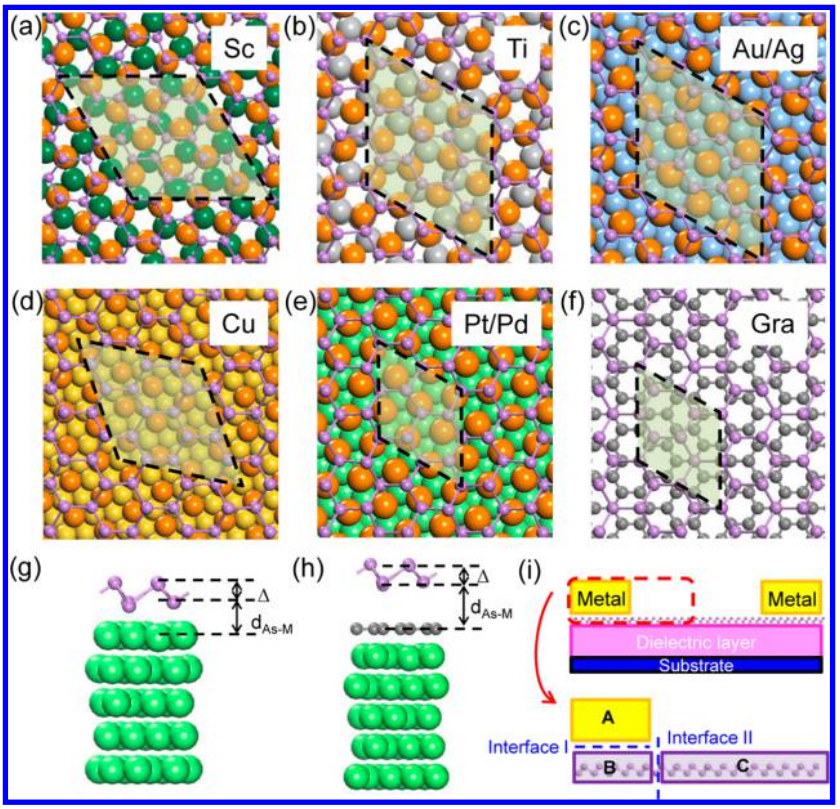

Figure 1. Optimized interfacial structures of ML arsenene contacted to various metal surfaces. Top views of ML arsenene on the (a) Sc(0001), (b) Ti(0001), (c) Au/Ag(111), (d) Cu(111), (e) Pt/Pd(111), and (f) graphene surfaces. The rhombus with black dashed edge shows the unit cell for each structure. Side views of ML arsenene-Pt contact (g) and ML arsenene-graphene-Pt contact (h) as examples. (i) Schematic diagram of a ML arsenene FET, in which the SB may be formed at two different interfaces (interface I and II). A–C represent different regions of the transistor.

transport and induces an extra contact resistance (R_c), which often degrades the device performance significantly. As is well-known, low R_c is not only critical for achieving a high on-current in 2D logic transistors but also critical for achieving high-frequency operation in 2D radiofrequency transistors[26] and large photoresponsivity in 2D photoconductors.[27,28] Actually the performance of most 2DSC SB FETs in the lab is often substantially below the theoretically predicted limits of their MOSFETs.[29] Undoubtedly, SB is a major concern for 2DSC applications.[29−32] To the best of our knowledge, no arsenene-metal contact has been investigated. Apparently, providing a prediction of the SB is very helpful for developing arsenene devices.

On the other hand, the photovoltaic (PV) effect of the SB at 2D material−metal interface is believed to play a significant role in photoresponse of 2D devices.[33] Many studies have found that the built-in electric field formed around the graphene−metal interfaces could realize the separation of excitons without an external bias, and the superior photocurrent density is revealed on the graphene−metal interfaces rather than the pure graphene region when illumination was shed on graphene devices.[34−37] PV effect in transition-metal dichalcogenides (TMDC) Schottky junctions also plays a role in photoresponse of TMDC devices considering the large area of metal contacts,[38−40] although photoconductive (PC) effect in the pure TMDC region is believed to be the main cause of the photogenerated carriers.[28,41] In view of the promising photoelectric applications of ML arsenene, a systematic study on SB in ML arsenene devices is needed.

In this paper, we systematically study the electrical contact properties of ML arsenene in top contact with elemental bulk metals spanning a wide work function range (Sc, Ti, Ag, Cu, Au, Pd, and Pt) by using *ab initio* band calculation combined with quantum transport simulations. After contact with bulk metals, the honeycomb structure of ML arsenene is intact, but its band structure is heavily hybridized, and ML arsenene undergoes a metallization. Lateral SB is always formed between the metalized ML arsenene and the channel ML arsenene due to a strong Fermi level pinning with a pinning factor of 0.33. ML arsenene forms an *n*-type Schottky contact with Sc, Ti, Ag, Cu, and Au electrodes with electron SB height (SBH) of 0.12, 0.21, 0.25, 0.35, and 0.50 eV, respectively, and forms a *p*-type Schottky contact with Pd and Pt electrodes with hole SBH of 0.75 and 0.78 eV, respectively. Substantial efforts such as using pure 2D metal electrodes,[42−45] phase engineering,[46,47] and 2D material-bulk metal hybrids[48−50] have been devoted to decreasing or even demolishing the SB in 2DSC devices because the Fermi level pinning effect can be reduced by the 2D van der Waals (vdW) contact due to the suppression of metal-induced gap states (MIGS). Finally, a barrier free hole injection is obtained by inserting a graphene between ML arsenene and bulk Pt metal.

Interface Model and Computational Methods. The optimized in-plane lattice constant and buckling distance of ML arsenene are a = 3.58 Å and d = 1.38 Å, respectively, in good agreement with the previous calculated values.[4,5,8,12] As the properties of arsenene are sensitive to its lattice parameter, we fix the lattice constant of ML arsenene to its optimized value and adjust the bulk metal and graphene lattice to be

DOI: 10.1021/acsami.7b08513
ACS Appl. Mater. Interfaces XXXX, XXX, XXX−XXX

Table 1. Calculated Interfacial Properties of ML Arsenene on the Metal Surfaces[a]

metal	mismatch (Å)	$d_{As\text{-}M}$ (Å)	d_{min} (Å)	E_b (eV)	W_M (eV)	W (eV)	Φ_V^e (eV)	Φ_V^h (eV)	$\Phi_{L,T}^e$ (eV)	$\Phi_{L,T}^h$ (eV)
Sc	3.84%	1.995	2.476	1.131	3.24	3.45	0	0	0.12	1.51
Ti	0.96%	2.110	2.534	1.357	4.32	4.40	0	0	0.21	1.41
Ag	3.02%	2.421	2.596	0.756	4.46	4.47	0	0	0.25	1.50
Cu	2.71%	2.318	2.380	0.864	4.84	4.45	0	0	0.35	1.25
Au	3.19%	2.446	2.555	0.808	5.23	4.90	0	0	0.50	1.11
Pd	1.64%	2.238	2.366	1.162	5.31	5.30	0	0	1.02	0.75
Pt	2.53%	2.180	2.424	1.149	5.82	5.26	0	0	0.85	0.78
Gr	3.06%	3.502	3.570	0.065	4.60	4.68	0.80($\Phi_{V,B}^e$)	0.80($\Phi_{V,B}^h$)	0.80	0.83
							0.80($\Phi_{V,T}^e$)	0.83($\Phi_{V,T}^h$)		
Gr_Pt	3.06%(Gr)/2.53%(Pt)	3.330	3.402	0.106	5.49	5.25	1.35($\Phi_{V,B}^e$)	0.25($\Phi_{V,B}^h$)	1.72	−0.10
							1.72($\Phi_{V,T}^e$)	−0.10($\Phi_{V,T}^h$)		

[a]The mismatch values are the lattice mismatch in metals. The equilibrium distance $d_{As\text{-}M}$ is the average distance between the bottom As atom layer and the relaxed positions of the topmost metal layer as depicted in Figure 1g,h. The minimum interatomic distance d_{min} is defined as the minimum atomic distance from As atoms to metal atoms. E_b is the binding energy per As atom between arsenene and a given metal. W_M and W are the calculated work functions for metal and arsenene-metal contact, respectively. The calculated work function of ML arsenene W_{As}, defined as the energy difference between the vacuum level and band gap center of the semiconductor, is 4.863 eV. $\Phi_{V/L,T/B}^{e/h}$ represents the vertical/lateral electron/hole SBH formed at interface I/II (Figure 1g), and the subscript T/B denotes the SBH derived from the quantum transport simulations (T)/ band structure analysis (B).

commensurate with ML arsenene. We use five layers of bulk metal atoms (Sc and Ti in (0001) orientation and Ag, Cu, Au, Pd, and Pt in (111) orientation) to model the metal surface because five-layer metal atoms can give converging properties of the contact system according to the convergence tests done in the previous studies.[51−56] The bottom three metal layers are kept fixed during the geometry optimization.

Restricting the in-plane lattice mismatch of metals within 4%, supercells of the contact junctions are generally large without a high symmetry stacking pattern (Figure 1a−f). The $(\sqrt{13} \times \sqrt{13})$ unit cell of Sc (0001) and Cu (111) faces is adjusted to the $(\sqrt{7} \times \sqrt{7})$ and $(2\sqrt{3} \times 2\sqrt{3})$ unit cell of ML arsenene, respectively; the $(\sqrt{13} \times \sqrt{13})$ unit cell of Ti (0001) and Au and Ag (111) faces is adjusted to the (3×3) unit cell of ML arsenene; and the $(\sqrt{7} \times \sqrt{7})$ unit cell of Pd and Pt (111) faces and (3×3) unit cell of graphene are adjusted to the (2×2) unit cell of ML arsenene. The most stable ML arsenene-metal top contact geometries are obtained by optimizing the structures from different initial configurations. The total energy is not sensitive to the relative interface positions in ML arsenene−bulk metal contacts, which is reasonable considering their low symmetry stacking patterns. ML arsenene-graphene-Pt hybrid contact is also constructed by inserting (3×3) unit cell of ML graphene between the optimized (2×2) ML arsenene−$(\sqrt{7} \times \sqrt{7})$ Pt superstructures (Figure 1h).

The ML arsenene device is built with different metal electrodes by utilizing the above optimized ML arsenene−metal junctions. It is noteworthy that in a device configuration there exist two interfaces as shown in Figure 1(i): the interface between the metal (region A) and 2DSC under the metal (region B), i.e., interface I, and the interface between the metal contacted 2DSC (region B) and 2DSC channel (region C), i.e., interface II.[52,57] In the weak hybridization type of top contacts, the SB is formed at interface I in the vertical direction and interface II in the lateral direction. In the strong hybridization type of junctions, ML arsenene−metal contact can be regarded as a new metal system, and the SB is formed at interface II in the lateral direction. The vertical SBH can be estimated from either the electronic or transport calculations, and the lateral SBH can only be estimated from the transport calculations.

We perform the geometry optimizations and electronic calculations with the projector-augmented wave (PAW) pseudopotential[58,59] and plane-wave basis set with a cutoff energy of 400 eV implemented in the Vienna *ab initio* simulation package (VASP).[60−63] A DFT-D dispersion-correction method of Grimme is used to describe vdW interactions. The dipole correction is adopted to get rid of the spurious interaction caused by the dipole moments of periodic images in direction perpendicular to the interface. The lattice constant of the supercell is fixed during the relaxation. The stopping criteria for the ionic relaxation are such that the remnant force on each atom is below 0.01 eV/Å and that the energy is converged to within 10^{-5} eV per atom. The Monkhorst−Pack[64] **k**-point mesh is sampled with a separation of about 0.10 and 0.03 $Å^{-1}$ in the Brillouin zone during the relaxation and electronic calculation periods, respectively. A vacuum buffer space of at least 20 Å is set.

The arsenene devices with different electrodes are simulated using the DFT coupled with the nonequilibrium Green's function (NEGF) method with single-ζ plus polarization (SZP) basis set, as implemented in the ATK 2016 package.[65] The Monkhorst−Pack **k**-point meshes for the central region and electrodes are sampled with $1 \times 50 \times 1$ and $1 \times 50 \times 50$, respectively. The temperature is set to 300 K. The transmission coefficient at k_y point (perpendicular to the transport z direction) and energy E is obtained by

$$T(k_y, E) = \mathrm{Tr}[\Gamma_L(k_y, E)G^r(k_y, E)G^a(k_y, E)\Gamma_R(k_y, E)] \quad (1)$$

where $G^{r(a)}$ is the retarded (advanced) Green function and $\Gamma_{L(R)}(k_y,E) = i(\sum_{L(R)}^{r}(k_y,E) - \sum_{L(R)}^{a}(k_y,E))$ is the level broadening due to left (right) electrode expressed in terms of the electrode self-energy $\sum_{L(R)}(k_y,E)$. The transmission function at a given energy $T(E)$ is averaged over 50 k_y-points in the irreducible Brillouin zone. Throughout the paper, the generalized gradient approximation (GGA) functional to the exchange-correction functional of the Perdew−Burke−Ernzerhof (PBE) is adopted.

Many body effects are not considered during evaluating the SBHs. In a device configuration, 2DSC is doped either by metal electrode or by gate, and electron−electron interaction is

DOI: 10.1021/acsami.7b08513
ACS Appl. Mater. Interfaces XXXX, XXX, XXX−XXX

greatly screened by doped carriers. Hence, the transport gap can be well described by the DFT-GGA method. With ML phosphorene taken as an example, the measured transport gap is 1.0 eV,[66] while the calculated DFT-GGA band gap, quasiparticle band gap, optical gap, and HSE (Heyd−Scuseria−Ernzerhof) band gap of the pristine phosphorene are 0.91,[55,67] 2.0−2.2,[25,68] 1.3−1.53,[25] and 1.5 eV,[67,69] respectively. Apparently, the DFT-GGA band gap is closest to the transport gap. Single electron theory is also a good approximation to the band edge positions, which has been proved in several 2DSC transistor simulations. For example, the calculated hole (electron) SBH of 0.26/0.19/0.20 (0.39/0.52/0.48) eV[43,59,60] in ML/bilayer/trilayer phosphorene FET with Ni electrode using DFT-GGA is consistent with the experimental value of 0.35/0.23/0.21 (0.64/0.48/0.40) eV.[66] The derived hole SBH of 0.30/0.18/0.21 eV in ML/bilayer/trilayer phosphorene FET with Ti electrode using DFT-GGA is in good accordance with the observed value of 0.21 eV[70] in ultrathin phosphorene FET with the same electrode.

RESULTS AND DISCUSSION

Bulk Metal Top Contacts. After structural optimization, the geometrical structure of ML arsenene is slightly distorted (Figures 1 and 5), but the honeycomb structural form of ML arsenene is maintained well on different metal substrates (Figure 1). The equilibrium interfacial distance $d_{\text{As-M}}$ is defined as the average vertical distance from the bottom As atom layer to the topmost bulk metal layer as shown in Figure 1g. The binding energy per interfacial As atom is defined as

$$E_b = (E_{As} + E_{metal} - E_{As-metal})/N_{As} \quad (2)$$

where E_{As}, E_{metal}, and $E_{As\text{-}metal}$ are the relaxed energies for ML arsenene, metal surface, and the combined system per supercell, respectively, and N_{As} is the number of As atoms per supercell. The adsorption of ML arsenene-bulk metal surfaces can be classified into weak chemical bonding and strong chemical bonding according to the interfacial distance and binding strength. Weak chemical bonding is formed in ML arsenene-Ag, Cu, and Au contacts with larger interfacial distance $d_{\text{As-M}}$ of 2.318−2.446 Å and smaller binding energy E_b of 0.756−0.864 eV, while strong chemical bonding is formed in Sc, Ti, Pd, and Pt contacts with smaller $d_{\text{As-M}}$ of 1.995−2.238 Å and larger E_b of 1.131−1.357 eV (Table 1).

Such a difference can be explained in terms of the different number of covalent bonds between metal and ML arsenene. Au, Ag, and Cu atoms have fully filled d-orbitals and half-filled s-orbitals, that is, they all have one unpaired s-electron. Therefore, Au, Ag, and Cu atoms form one covalent bond with arsenene. Pt atom ($5d^9 6s^1$) has one unpaired d-electron and one unpaired s-electron, and Pd atom also has a similar electronic configuration when forming into bulk in terms of Mulliken population analysis. Thus, Pt and Pd atoms form two covalent bonds with arsenene. The electronic configurations of Sc ($3d^1 4s^2$) and Ti ($3d^2 4s^2$) atoms are respectively transformed to $3d^2 4s^1$ and $3d^3 4s^1$ approximately in the contact system, and thus Sc (Ti) forms three (four) covalent bonds with arsenene. Besides, d-orbitals are more localized than s- and p-orbitals, which usually results in a shorter bond length and a higher bond energy. As a result, Sc, Ti, Pd, and Pt have a stronger binding with ML arsenene than Au, Ag, and Cu due to the more d-orbital-related covalent bonds.

It is interesting to compare the binding strength of different elemental 2D materials with metal. After unifying the definition of the binding energy to per 2D material atom, the bindings of ML arsenene with the same bulk metal are much stronger than those of the light group IVA 2D materials, such as ML graphene (0.03−0.08 eV)[71] and graphdiyne (0.09−0.23 eV)[53] by about 1 order of magnitude and its group VA cousin ML black phosphorene (0.22−0.45 eV)[55] by twice, but are comparable with the heavy group IVA 2D material, stanene (0.84−1.63 eV)[72] and weaker than the heavy group VA 2D material, bismuthene (1.09−1.98 eV).[73] These bindings are slightly stronger than those of the middle group IVA 2D materials, such as silicene and germanene with the weak chemical bonding type of metals (0.34−0.63 eV) but are comparable with those of silicene and germanene with the strong chemical bonding type of metals (1.17−1.74 eV).[74,75]

The minimum interatomic distance d_{min}, which is defined as the minimum atomic As−metal distance, is rather insensitive to the bulk metal species, varying from 2.366 to 2.596 Å as listed in Table 1. Electron localization function (ELF) allows us to directly appraise the chemical interaction between atoms, whose value represents the localization degree of electrons. According to the analysis of ELF in Figure S1, the magnitudes of the ELF values between As-bulk metal atom pairs are in the range of ∼0.40−0.65, identifying an apparent covalent bond character between arsenene and all the metal substrates. The electron density redistribution at the interface is also studied by calculating the electron density difference after the formation of the junction

$$\Delta\rho = \rho_{As-metal} - \rho_{As} - \rho_{metal} \quad (3)$$

Averaged $\Delta\rho$ along the direction perpendicular to the interface ($\Delta\rho_z$) for ML arsenene-Pt is given in Figure S2(a) as a representation. The amount of shared density at the interface is high, so that the bonds can be described as having a large covalent character. The innermost Pt and As atom layers have some charges and electrons, respectively, so the bonds also have a considerable ionic character.

The band structures of ML arsenene and the contact systems are shown in Figure 2. Free standing ML arsenene has a band gap of 1.60 eV at the PBE level, consistent with the reported DFT value of 1.50−1.76 eV.[4,5,8,12] The valence and conduction bands of ML arsenene are heavily distorted due to the strong band hybridization in all the studied ML arsenene-bulk metal contacts, indicative a formation of covalent bond, a fact consistent with the previous analyses. E_f crosses the arsenene-derived band, indicating a metallization of ML arsenene at the interface. To further verify the hybridization, partial density of states (PDOS) of ML arsenene on the bulk metal surfaces are provided in Figure S3. After contact with bulk metals, the original band gap of ML arsenene vanishes. Therefore, Ohmic injection of carriers is realized in the vertical direction for all the studied junctions.

Lateral SB is possibly formed between the metallized ML arsenene and channel ML arsenene in a FET. We study the lateral SB through the quantum transport simulation of a ML arsenene device with different bulk metal electrodes (Figure 3a). The local density of states (LDOS) and transmission spectra of the simulated ML arsenene transistors are provided in Figure 3b−h. We can see a transmission gap around 1.65 eV in all ML arsenene transistors, comparable with the previous calculated band gap of ML arsenene (1.60 eV). Lateral SBHs are determined from the energy difference between E_f of the transistor system and the conduction band minimum (CBM) or valence band maximum (VBM) of the channel ML arsenene

DOI: 10.1021/acsami.7b08513
ACS Appl. Mater. Interfaces XXXX, XXX, XXX−XXX

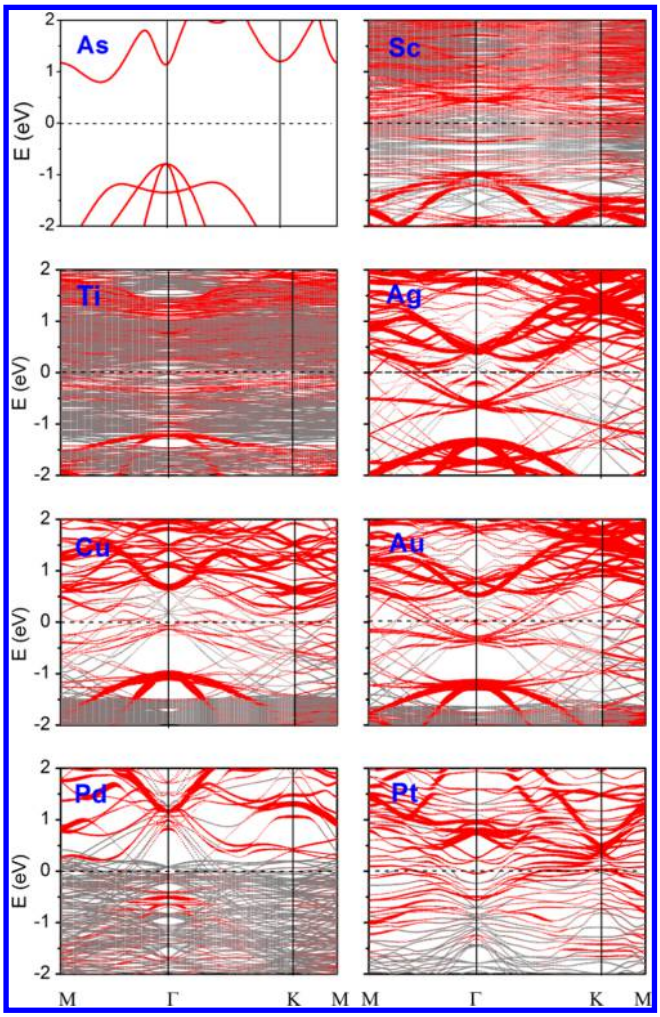

Figure 2. Band structures of ML arsenene and ML arsenene-Sc, -Ti, -Ag, -Cu, -Au, -Pd, and -Pt contacts, respectively. Gray line: bands of metal surface; red line: bands of ML arsenene. The line width is proportional to the weight. The Fermi level is set at zero.

at interface II. No Ohmic contact is found. In terms of the LDOS, Schottky contact is *n*-type with $\Phi^{e}_{L,T}$ = 0.12, 0.21, 0.25, 0.35, and 0.50 eV, respectively, when using Sc, Ti, Ag, Cu, and Au electrodes, and is p-type with $\Phi^{h}_{L,T}$ = 0.75 and 0.78 eV, respectively, when using Pd and Pt electrodes. The band bending of the channel ML arsenene is generally observed, indicating a built-in potential $\Delta\varphi$ between the source/drain and channel region induced by the charge transfer at interface II. Due to this band bending of the channel, the lateral electron (hole) SBH slightly deviates from the energy difference between E_f and CBM (VBM) of the transmission spectrum. Apparent MIGS occur at interface II in the ML arsenene FETs as indicated in Figure 3, which can induce Fermi level pinning between the source/drain and the ML arsenene channel. MIGS also reduce the effective channel length and furthermore degrade the device performance.

To provide a clear picture, the SBHs of ML arsenene-bulk metal contacts are summarized in Figure 4a. From left to right, ML arsenene is gradually changed from n- to p-type doping, which can be utilized to build p−n junctions and complementary logic designs. The electron SBHs of ML arsenene vs the metal work function are plotted in Figure 4b and compared with ML and multilayer MoS_2,[29,30,52] and ML WSe_2.[57] The points in Figure 4b are rather scattered. The cause lies in the fact the metal contacted ML arsenene undergoes a metallization, and the degree of correlation between the lateral SBH (at interface II between the metallized arsenene and the channel arsenene) and the work function W_M of pure bulk metals is therefore weakened. We apply a linear fit to the data to coarsely determine the divergence from the Schottky-Mott model. The slope is referred to as pinning factor *S*. $S = 1$ means following the Schottky-Mott model and no Fermi level pinning, and $S = 0$ indicates a complete Fermi level pinning. The calculated pinning factor is 0.33 for the ML arsenene-bulk metal contacts, implying a strong Fermi level pinning effect. Such an *S* appears comparable with the theoretically predicted $S = 0.27$ in the MoS_2 case and $S = 0.32$ in the WSe_2 case. However, the theoretical SBHs for the ML arsenene-bulk metal contacts are derived from the quantum transport simulation of the transistor, where both the couplings at interface I and II are taken into consideration, whereas the theoretical SBHs in MoS_2 and WSe_2-metal contacts are derived from the band analysis, where the coupling between the metal contacted MoS_2/WSe_2 and the channel MoS_2/WSe_2 (namely at interface II) is not considered. Therefore, the calculated Fermi level pinning effect is underestimated for the MoS_2- and WSe_2-metal contacts. Actually, the measured pinning factor *S* of 0.10[17,18] is indeed apparently smaller than the theoretical value of 0.27 in the MoS_2-metal contact. Another cause of the quite small measured pinning factor in the MoS_2-metal contact is the existence of the defects in the experimental example,[76] which always increases the Fermi level pinning effect. The Fermi level pinning effect in ML arsenene-bulk metals is illustrated more clearly in Figure 4c, where the Fermi level of the contact is pinned in a range between the ∼0.1 eV below the CBM and 0.75 eV above the VBM of ML arsenene. The origin of this pinning is attributed to the presence of the apparent MIGS in all the arsenene-metal contacts (Figure 3).

Tunneling barrier (TB), another figure of merit of a contact, often exists in 2DSC−metal interfaces. Tunneling through a TB deteriorates the carrier injection efficiency and thus degrades the device performance. Here, the height of TB is defined as the energy difference between E_f of the system and the potential energy of the interface gap. There is no TB for all our studied ML arsenene-bulk metal contact electrodes (Figure 5a−g), which is consistent with the strong band hybridization between ML arsenene and bulk metals. Apparently, ML arsenene-bulk metal contacts have perfect tunneling transmission.

Graphene Top Contact. Direct deposition of bulk metals on 2DSCs can usually result in a strong Fermi level pinning due to the MIGS and experimentally introduced defect states and thereby a finite SB and a relatively large R_c. Alternatively, graphene can be used as a contact material and the resulting nondamaging vdW contact provides an atomically sharp and ultraclean interface that minimizes MIGS and defects.[29] There are three types of interface geometries in a graphene contacted ML arsenene transistor (Figure 6a): coplanar stack contact, staggered contact, and hybrid contact. In the former two types, the metal contact is far away from the 2DSCs, and ML arsenene integrates with pure graphene through a vdW interaction with a calculated equilibrium interfacial distance $d_{As\text{-}M}$ of 3.502 Å, minimum atomic distance d_{min} of 3.570 Å, and binding energy E_b of 0.065 eV. The band structure of the ML arsenene-graphene contact can be seen as a combination of well-preserved band structures of graphene and ML arsenene almost without hybridization (Figure 6b). The vertical hole (electron)

DOI: 10.1021/acsami.7b08513
ACS Appl. Mater. Interfaces XXXX, XXX, XXX−XXX

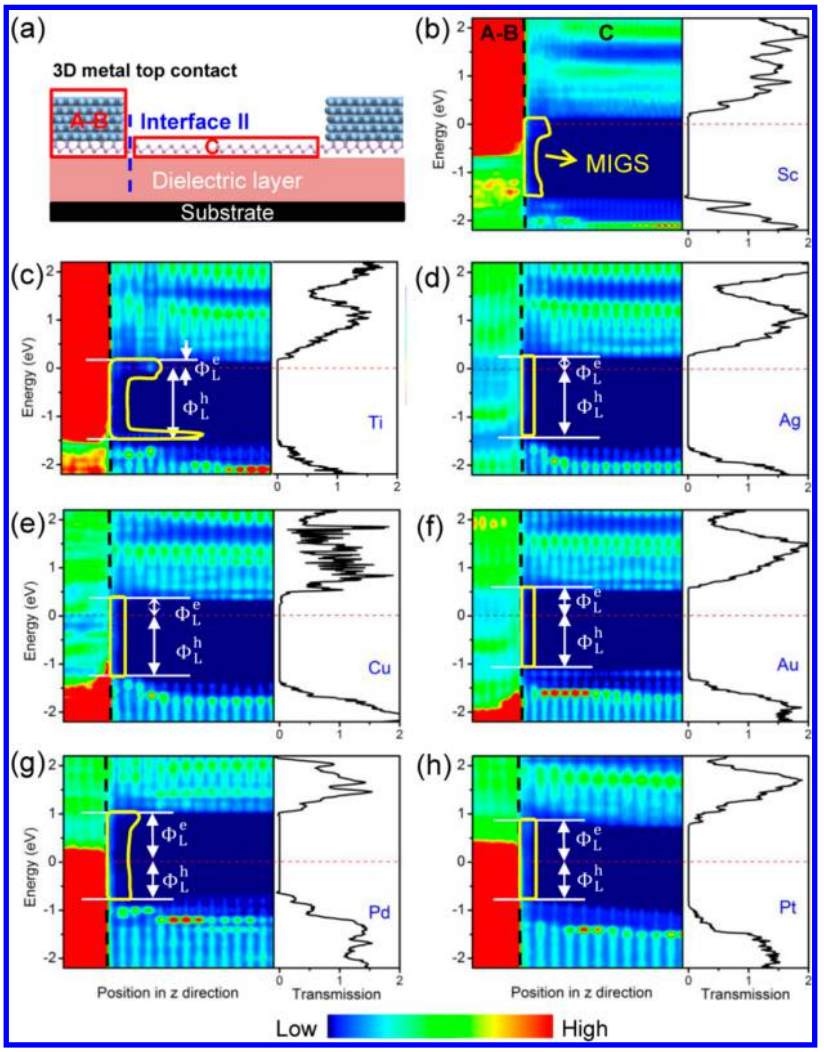

Figure 3. Simulation of the ML arsenene FETs with different bulk metal electrodes. (a) Schematic two-probe model. (b–h) Zero-bias local density of states (LDOS) (left panel) and transmission spectra (right panel) of the transistors with different electrodes. The upright black dashed lines indicate the boundary of ML arsenene-bulk metal (region A–B) and the uncontacted ML arsenene channel (region C). The color scale is shown below the plot. Yellow closed area indicates the region with MIGS. The Fermi level is set at zero.

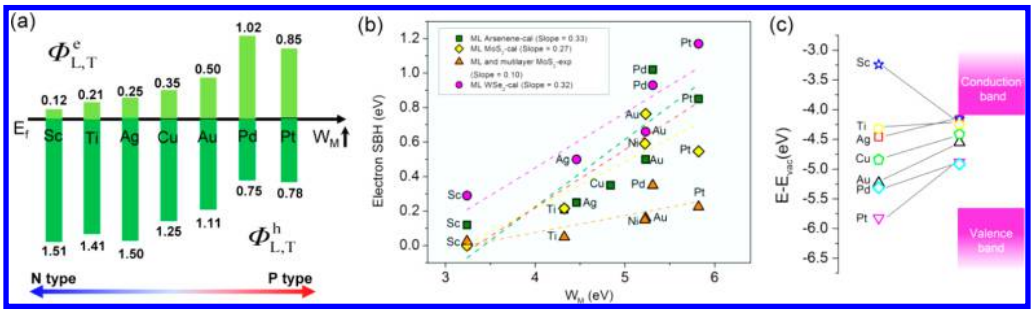

Figure 4. (a) Lateral electron and hole SBHs of the ML arsenene FETs with bulk metal contact obtained from the quantum transport simulation. (b) Comparison of the electron SBHs in ML arsenene, ML and multilayer MoS_2 [29,30,52] and ML WSe_2 [57] FETs against the metal work function. (c) Illustration of Fermi level pinning in the ML arsenene FETs.

SBH $\Phi_{V,B}^{h(e)}$ can be derived as the energy difference of the VBM (CBM) of ML arsenene and E_f of the junction from the band structure. $\Phi_{V,B}^{e}$ and $\Phi_{V,B}^{h}$ are nearly equal with a value of about 0.8 eV. The PDOS of As electronic orbitals are also provided in the right panel of Figure 6b, and no MIGS exist in the band gap.

ML arsenene transistor with pure graphene electrode is simulated at zero bias and zero gate voltage. The LDOS projected on ML arsenene and transmission spectrum of the simulated ML arsenene transistor with pure graphene electrode are shown in Figure 6c. The conduction and valence band edges of ML arsenene are flat in both the electrode and channel regions; therefore the vertical and lateral SBHs in terms of the LDOS are identical and the built-in potential $\Delta\varphi$ is zero at interface II. The vertical and lateral SBHs are quite close to those from the band analysis of the electrode with $\Phi_{V/L,T}^{e}$ of

DOI: 10.1021/acsami.7b08513
ACS Appl. Mater. Interfaces XXXX, XXX, XXX–XXX

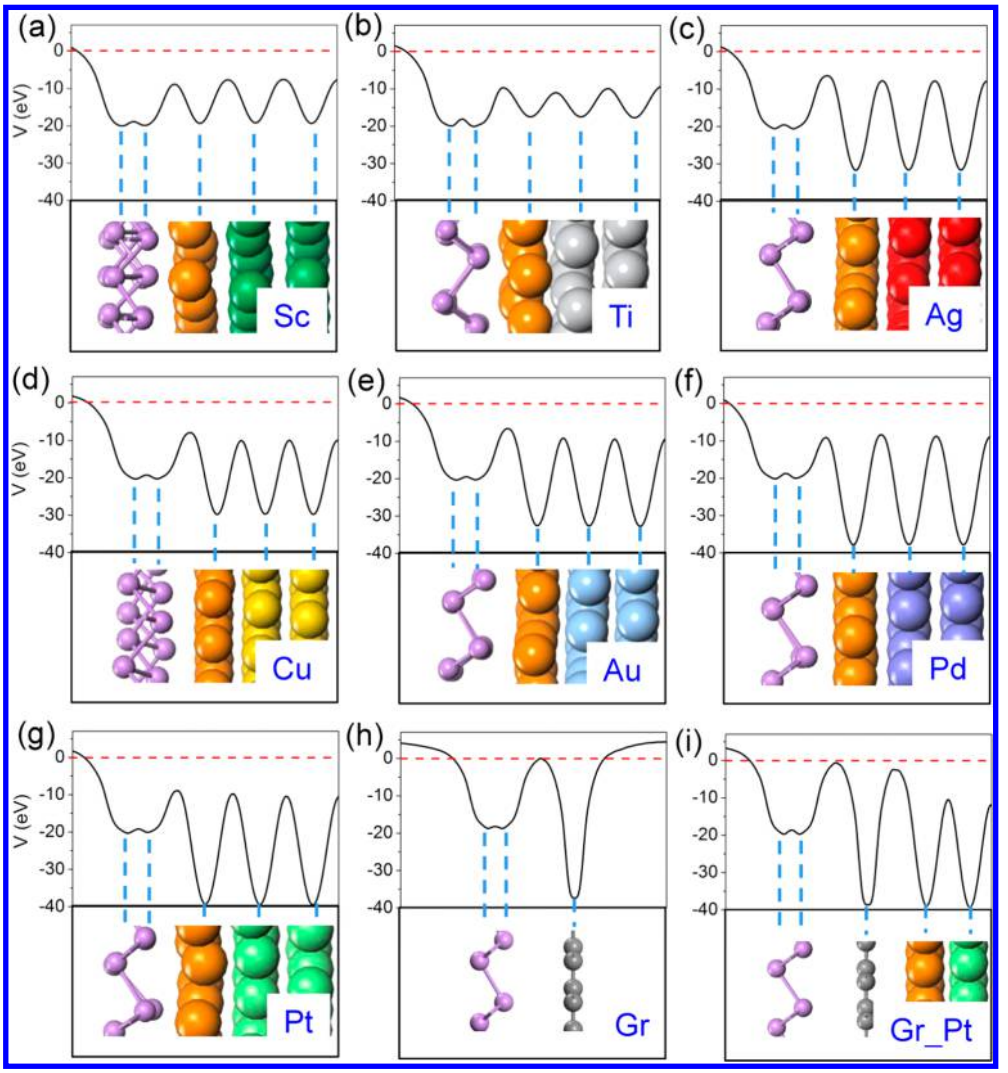

Figure 5. Plane-averaged total potential V along the direction perpendicular to the (a–g) ML arsenene-bulk metal, (h) -graphene, and (i) -graphene-Pt interfaces. The Fermi level is set at zero. The innermost bulk metal layer is denoted in orange.

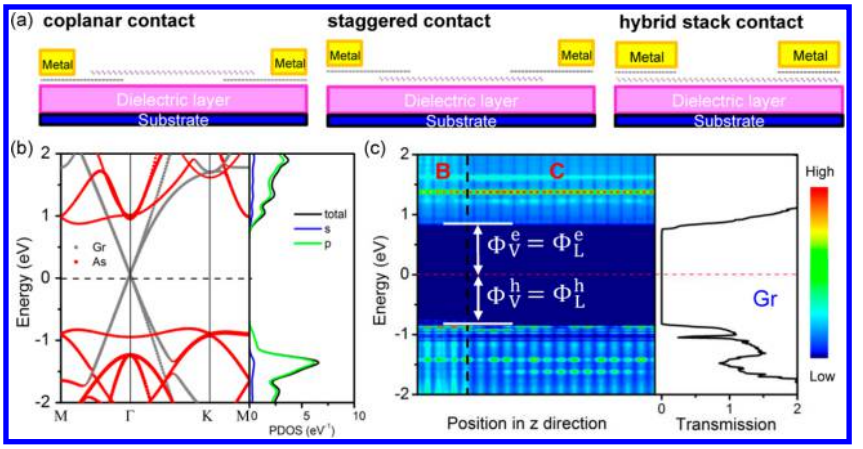

Figure 6. (a) Schematic diagrams of three types of graphene contacts in a ML arsenene device: coplanar contact, staggered contact, and hybrid stack contact. (b) Band structure and PDOS of As orbitals for the ML arsenene-pure graphene contact. (c) Zero-bias LDOS projected on ML arsenene and transmission spectrum of the ML arsenene transistor with pure graphene electrode. The upright black dashed line indicates the boundary of graphene contacted ML arsenene (region B) and the uncontacted ML arsenene channel (region C). The Fermi level is set at zero.

0.80 eV and $\Phi^h_{V/L,T}$ of 0.83 eV. As shown in Figure 6c, no MIGS is observed in the band gap of ML arsenene under the graphene electrode (region B), which is consistent with the electronic calculation analysis. There are also no MIGS at interface II. Owing to the absence of MIGS, E_f of graphene and ML arsenene will not be pinned, and the SBH is subject to a

DOI: 10.1021/acsami.7b08513
ACS Appl. Mater. Interfaces XXXX, XXX, XXX–XXX

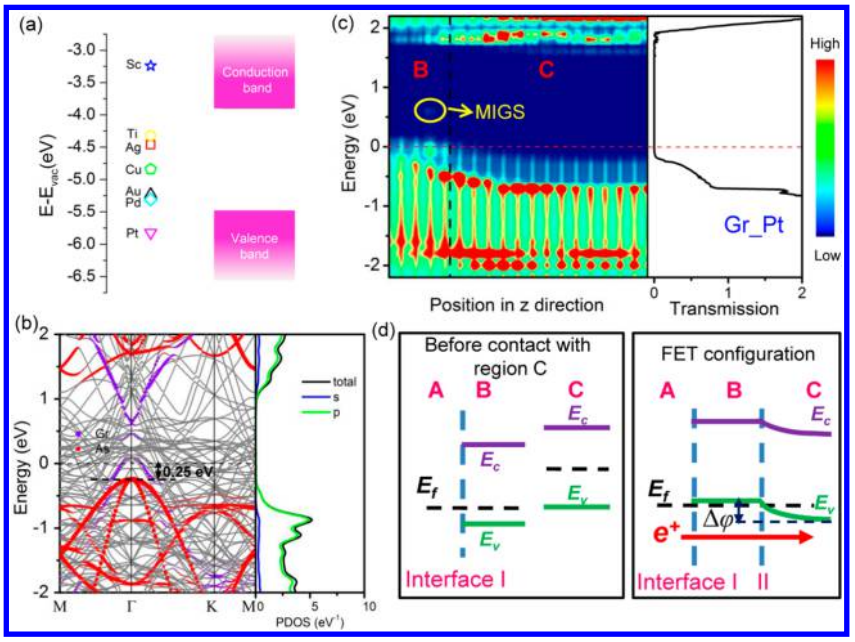

Figure 7. (a) Band alignment between graphene contacted ML arsenene and bulk metals. (b) Band structure and PDOS of As orbitals for the ML arsenene-graphene-Pt contact. Gray line: bands of Pt metal; red line: bands of ML arsenene; purple line: bands of graphene. The red and purple line width is proportional to the weight. (c) Zero-bias LDOS projected on the ML arsenene (left panel) and transmission spectrum (right panel) of transistor with hybrid graphene-Pt electrode. The upright black dashed line indicates the boundary of the ML arsenene under the hybrid contact (region B) and the uncontacted ML arsenene channel (region C). (d) Band diagrams of the isolated ML arsenene-graphene-Pt hybrid electrode and channel and their combined system in a FET. E_c and E_v denote the conduction and valence band edges of the ML arsenene, respectively.

modulation by gates. Therefore, an Ohmic contact for both electron and hole injections can be expected in the ML arsenene FET with graphene electrode under a proper gate voltage.[42−44,77]

In the third type of interface geometry (hybrid contact, see Figure 6a), graphene can be regarded as a buffer layer between 2DSC and bulk metal electrodes. We compare the different bulk metal work functions with the CBM and VBM of ML arsenene after contacted with ML graphene in Figure 7a. Sc and Pt are promising candidates to achieve n-type and p-type Ohmic contacts because their Fermi levels are above the CBM and below the VBM of ML arsenene, respectively. Here we select Pt electrode to study due to its relative small supercell and thereby less computational resources consumed. The calculated equilibrium interfacial distances $d_{As\text{-}M}$ is 3.330 Å and minimum atomic distance d_{min} is 3.402 Å, typical of vdW spacing. The binding energy E_b is ∼0.1 eV between ML arsenene and graphene-Pt hybrid electrode, slightly larger than the 0.065 eV in the pure graphene contact, which may be caused by the larger dipole interaction induced by the additional Pt contact. The electron density change $\Delta\rho_z$ for ML arsenene-graphene-Pt contact is also provided in Figure S2(b). Electrons are transferred from graphene to the interface gap with ML arsenene and metal Pt, but the As atom layers have some extra positive charges.

The band structure and PDOS of ML arsenene are well preserved by the buffer layer graphene, as shown in Figure 7b. Compared with Figure 6b, the valence band of graphene is slightly destroyed due to the hybridization with metal Pt. No apparent MIGS exist at interface I in the vertical direction. A vertical hole SBH $\Phi^h_{V,B}$ of 0.25 eV is observed, which is against our goal of realization of a p-type Ohmic contact. The rise of E_f of metal Pt upon contact is responsible for the appearance of the hole SB We attribute the rise of E_f of metal Pt upon contact to the fact that metal Pt accepts electrons from graphene because the work function of metal Pt (5.82 eV) is larger than that of graphene (4.60 eV) (Table 1).

The LDOS projected on ML arsenene in the transistor with graphene-Pt hybrid electrode is shown in Figure 7c. The CBM and VBM of ML arsenene under graphene-Pt hybrid electrode are flat (region B), suggestive of identical vertical and lateral hole SBHs. E_f is below the VBM of ML arsenene at both interface I and II, and we have $\Phi^h_{V,T} = \Phi^h_{L,T} = -0.10$ eV in terms of the LDOS. Therefore, a p-type Ohmic contact is realized by using the graphene-Pt hybrid electrode. The VBM of ML arsenene bends downward from 0.10 eV at interface II to −0.20 eV at the central channel region. Because of the apparent band bending of 0.3 eV near interface II, and the energy difference between E_f and the VBM of the transmission spectrum (∼0.20 eV, right panel of Figure 7c) is not equal to the hole SBH.

It is noteworthy that the vertical SBH given by the energy band calculation based on isolated electrode model ($\Phi^h_{V,B}$ = 0.25 eV) is not equal to the one given by the quantum transport simulation of the transistor ($\Phi^h_{V,T}$ = −0.10 eV) because of the band bending at interface II. This band bending arises from the electrons transferred from the channel arsenene (region C) to the arsenene under the graphene-Pt electrode (region B) because E_f of channel ML arsenene is higher than E_f of the electrode (left panel of Figure 7d). A built-in field is formed at interface II and it elevates the bands of ML arsenene at region B by a built-in potential $\Delta\varphi$ of about 0.30 eV, which thus decreases $\Phi^h_{V,B}$ from 0.25 eV to −0.10 eV (right panel of Figure 7d). Therefore, caution must be taken when using the energy band calculation based on isolated electrode model to estimate the vertical and lateral SBHs of a FET even if the electrode and the 2DSC only has a weak vdW coupling although such an estimation is widely adopted.

DOI: 10.1021/acsami.7b08513
ACS Appl. Mater. Interfaces XXXX, XXX, XXX−XXX

A small amount of MIGS appears at interface I and no MIGS exists at interface II after the graphene insertion between Pt electrode and ML arsenene in terms of the LDOS of the FET configuration (Figure 7c). The suppression of MIGS greatly lightens the Fermi level pinning. The band bending at interface II and absence of MIGS account for the appearance of the Ohmic contact upon inserting the graphene buffer layer. Compared with the case of pure bulk Pt electrode (Figure 3h), through inserting the buffer layer graphene, a large lateral SBH of 0.78 eV is dismissed and a barrier free hole injection is realized in the ML arsenene transistor. Therefore, the lowest contact resistance and highest device performance can be expected in the ML arsenene FET with graphene-Pt hybrid electrode. In other words, the predicted excellent device performance of SB-free ML arsenene MOSFET[3,4] is likely to be realized in the ML arsenene FET with graphene-Pt hybrid electrode.

It is previously believed that tunneling through the vdW gap between graphene and 2DSC like TMDCs (~3.3 Å) may lead to higher R_c, and the calculation of ML graphene insertion between the ML MoS_2−Sc interface did show a tunneling barrier of 1.29 eV high and 0.41 Å wide, which results in a 62% tunneling probability by using the square potential barrier model.[50] According to our total potential calculation, the potential of the vdW gap is just located at E_f in the ML arsenene-graphene and -graphene-Pt contacts (Figure 5h,i). Therefore, the TB is zero at our ML arsenene-graphene and -graphene-Pt interfaces for the carriers at E_f. The carriers below E_f will still face a small TB, whose height is the difference of its energy and E_f.

Here only ML graphene is considered as 2D metal electrode and 2D buffer layer in the ML arsenene FET. The absence of the MIGS and a weak Fermi level pinning can also be expected by using other 2D metals as electrode such as 1T and 1T′ MoX_2 and WX_2, group VB MX_2 (M = V, Nb, and Ta, X = S, Se, and Te), and so on. The buffer layer between bulk metal with high (low) work function and ML arsenene can also use other 2D materials, such as insulating ML BN layer. As a group VA-ene, ML antimonene shares similar electronic properties with ML arsenene. Therefore, our study may also provide some guidelines for designing a low-R_c ML antimonene-metal contact.

To evaluate the spin−orbital coupling (SOC) effect in the contacts, the band structures of ML arsenene and ML arsenene-Pt contact after considering the SOC are provided in Figure S4. The band gap of ML arsenene is slightly reduced from 1.60 to 1.48 eV with the SOC, which is the same as that calculated by Xu et al.[6] and slightly smaller than the value of 1.59 eV calculated by Sun et al.[9] The SOC correction is as small as 0.12 eV in Xu's[6] and our work and negligible (0.01 eV) in Sun's work.[9] The reduction of the band gap generally results in the reduction of both the vertical and lateral SBHs. ML arsenene is strongly metallized after contact with the Pt electrode, and therefore Ohmic contact is formed in the vertical direction even with the SOC effect (Figure S4(b)). It is too expensive to perform a direct calculation of the lateral SBH through the *ab initio* quantum transport simulation with the SOC effect. However, the reduction of the lateral SBH are expected to be much less than the band gap reduction of 0.12 eV by the SOC in the bulk metal contacts since there is a strong Fermi pinning effect. In the graphene-Pt hybrid contact, vertical and lateral Ohmic contacts will be preserved owing to the slightly reduced band gap of channel ML arsenene.

In reality, when ML arsenene contacts with bulk metal, the bulk metal maintains its original lattice constant and the lattice constant of ML arsenene is adjusted to that of the metal. In our transistor simulations, because the channel ML arsenene is not strained by the metal and keeps its pristine structure, we have to choose to strain the metal electrode to fit the ML arsenene in the source and drain regions while constructing the 2D device model so that the periodic boundary condition can be used in y direction. The electrical properties of the contact in which ML arsenene is strained to fit the bulk metal Pt are also investigated. The band structure of the strained arsenene is strongly hybridized with that of Pt and the band gap vanishes (Figure S5(a)). Therefore, ML arsenene is metallized by the bulk metal Pt and Ohmic injection is still realized in the vertical direction in this matching strategy. The work function of the strained ML arsenene-Pt contact is 5.32 eV, comparable with the 5.26 eV in the ML arsenene-strained Pt contact. The TB in the vertical direction is still zero (Figure S5(b)). The lateral SB is formed between the metal contacted ML arsenene and unstrained channel arsenene. Considering the almost unchanged electronic properties of the ML arsenene-Pt contact using the two different matching strategies, the lateral SBH should also not be affected much.

So far the reports about 2D arsenene growth are quite limited owing to its toxicity. Expect the successful synthesis of multilayer arsenene nanoribbons, a thin layer of gray arsenic was manufactured by molecular beam expitaxy.[78] We also anticipate 2D arsenene can be obtained by exfoliation, van der Waals epitaxy growth, and molecular beam epitaxy as its Sb-analogue antimonene.[16−22] The kinetic and thermodynamic stability of free-standing ML arsenene has been studied through phonon frequency calculations of the optimized atomic structures together with *ab initio* high-temperature MD simulations.[2,7] There are no imaginary frequencies in phonon calculations of ML arsenene, which implies its stability at low temperatures. During the MD calculations at temperature as high as 1000 K, its structure maintains its form, except for thermally induced deformation; no bond breaking or clustering occurs. So far, we do not find any report about the stability of ML arsenene in the air. Its bulk phase gray arsenic will be slowly oxidized upon exposure to air and eventually forms a black surface layer. ML arsenene is expected to be degraded in the air more quickly than its bulk phase in light of the extremely high surface-to-volume ratio. The relative stability of ML arsenene versus ML black phosphorene in the air is unknown.

Our study focuses on the perfect ML case to provide a basic guide for experiments in the ideal situation. However, surface defects are unavoidable in the experimental process. The first-principles calculations done by Sun et al.[9] reveal that the band gap of ML arsenene is sufficiently reduced to 1.24, 0.10, 0.97, 1.42, and 0.0 eV by the SW, SV, DV of 5|8|5, DV of 555|777, and adatom defects, respectively. Therefore, the vertical and lateral SBHs of the contact with defective regions will be also significantly reduced especially for the SV and adatom defects. It has been proven in MoS_2 FETs that the presence of even low concentrations of defects dominates the observed Schottky barrier both from the experimental and theoretical perspectives, and the performance will be increased as the areal percentage of defects in the junction is increased.[79] Therefore, the performance of the ML arsenene device can even be improved in terms of the reduced SBH. On the other hand, the defects in the channel region may serve as scattering centers and are detrimental to the device properties in this aspect.

DOI: 10.1021/acsami.7b08513
ACS Appl. Mater. Interfaces XXXX, XXX, XXX−XXX

As the thickness of arsenene is increased from ML to bilayer, the band gap is sufficiently reduced from 2.49 to 0.37 eV at the HSE06 level of theory.[2] Therefore, the SBH of bilayer arsenene-metal contact should be greatly reduced compared with that of ML arsenene in contact with the same metal. Smaller SBH means lower contact resistance in the BL arsenene device. However, bilayer arsenene is not suitable for logic device applications because a semiconducting channel with band gap smaller than 0.4 eV is unable to offer excellent switching capability to compete the current silicon MOSFETs (on−off ratio of between 10^4 and 10^7).[80,81] As for arsenene with thickness above trilayer, they are metallic due to the fact that the 4p orbitals cross the Fermi level at several points in the Brillouin zone.[2]

The SBH between arsenene and different metals could be measured experimentally by analyzing temperature dependency of the electrical current of the corresponding transistors. The current density injected through a SB is

$$I_{2D} = WA^*_{2D}T^{3/2}\exp\left(-\frac{q\Phi_B}{kT}\right)\exp\left(\frac{qV_D}{kT}\right) \quad (4)$$

$$A^*_{2D} = \frac{q\sqrt{8\pi m^* k^3}}{h^2} \quad (5)$$

$$\Phi_B = \frac{k}{q}\left[\frac{\Delta \ln(I_{2D}/T^{3/2})}{\Delta T^{-1}}\right] \quad (6)$$

After measuring the current as a function of the temperature under fixed V_D, the SBH can be extracted from the slop of a linear fit to ln $(I_{2D}/T^{3/2})$ as a function of $1/T$ using eq 6.

CONCLUSION

We provide the first comparative study of the electrical contact properties of ML arsenene with bulk metals, 2D graphene, and graphene-Pt hybrid electrodes by using *ab initio* energy band calculations and quantum transport simulations. A Schottky barrier is always formed in our studied common bulk metal contacts owing to the strong Fermi level pinning effect (pinning factor S = 0.33) induced by MIGS. The Schottky contact is n-type in ML arsenene-Sc, -Ti, -Ag, -Cu, and -Au junctions and p-type in ML arsenene-Pd and -Pt junctions. The MIGS are greatly depressed by using 2D metal graphene and graphene-Pt hybrid electrode, and barrier-free hole (or electron) injection can be realized. This fundamental study gives a deep insight into ML arsenene−metal interfaces and provides a theoretical guidance for the selection of metal electrodes in ML arsenene devices.

ASSOCIATED CONTENT

Supporting Information

The Supporting Information is available free of charge on the ACS Publications website at DOI: 10.1021/acsami.7b08513.

Benchmark of the performance of ML arsenene MOSFETs against other 2DSC FETs; cross sections of the ELF for different ML arsenene-metal junctions; electron density differences after the formation of arsenene-Pt and arsenene-graphene-Pt contacts, PDOS of As electron orbitals for different ML arsenene-bulk metal contacts; band structures of ML arsenene and ML arsenene-Pt contact with the SOC effect; and band structure and plane-averaged total potential V of the ML arsenene-Pt contact in which ML arsenene is strained to fit the bulk metal Pt (PDF)

AUTHOR INFORMATION

Corresponding Authors

*E-mail: wangyangyang@qxslab.cn.
*E-mail: panfeng@pkusz.edu.cn.
*E-mail: jinglu@pku.edu.cn.

ORCID

Yangyang Wang: 0000-0003-3992-3796
Xiuying Zhang: 0000-0002-7393-9567
Ying Guo: 0000-0002-3039-9425
Feng Pan: 0000-0002-8216-1339

Author Contributions

#These authors contributed equally to this work.

Notes

The authors declare no competing financial interest.

ACKNOWLEDGMENTS

This work was carried out at National Supercomputer Center in Tianjin, and the calculations were performed on TianH2-1 (A). The work was supported by the National Natural Science Foundation of China (No. 11704406/11274016/11474012/11674005/11274233), National Materials Genome Project (2016YFB0700600), and the National Basic Research Program of China (No.2013CB932604/2012CB619304/2016YFA0301300).

REFERENCES

(1) Pumera, M.; Sofer, Z. 2D Monoelemental Arsenene, Antimonene, and Bismuthene: Beyond Black Phosphorus. *Adv. Mater.* **2017**, *29*, 1605299.

(2) Zhang, S.; Yan, Z.; Li, Y.; Chen, Z.; Zeng, H. Atomically Thin Arsenene and Antimonene: Semimetal−Semiconductor and Indirect−direct Band-gap Transitions. *Angew. Chem., Int. Ed.* **2015**, *54*, 3112−3115.

(3) Pizzi, G.; Gibertini, M.; Dib, E.; Marzari, N.; Iannaccone, G.; Fiori, G. Performance of Arsenene and Antimonene Double-gate MOSFETs from First Principles. *Nat. Commun.* **2016**, *7*, 12585.

(4) Wang, Y.; Huang, P.; Ye, M.; Quhe, R.; Pan, Y.; Zhang, H.; Zhong, H.; Shi, J.; Lu, J. Many-body Effect, Carrier Mobility, and Device Performance of Hexagonal Arsenene and Antimonene. *Chem. Mater.* **2017**, *29*, 2191−2201.

(5) Zhu, Z.; Guan, J.; Tománek, D. Strain-induced Metal-semiconductor Transition in Monolayers and Bilayers of Gray Arsenic: A Computational Study. *Phys. Rev. B: Condens. Matter Mater. Phys.* **2015**, *91*, 161404.

(6) Xu, W.; Lu, P.; Wu, L.; Yang, C.; Song, Y.; Guan, P.; Han, L.; Wang, S. Electronic and Optical Properties of Arsenene Under Uniaxial Strain. *IEEE J. Sel. Top. Quantum Electron.* **2017**, *23*, 214−218.

(7) Kecik, D.; Durgun, E.; Ciraci, S. Stability of Single-layer and Multilayer Arsenene and their Mechanical and Electronic Properties. *Phys. Rev. B: Condens. Matter Mater. Phys.* **2016**, *94*, 205409.

(8) Kamal, C.; Ezawa, M. Arsenene: Two-dimensional Buckled and Puckered Honeycomb Arsenic Systems. *Phys. Rev. B: Condens. Matter Mater. Phys.* **2015**, *91*, 085423.

(9) Sun, X.; Liu, Y.; Song, Z.; Li, Y.; Wang, W.; Lin, H.; Wang, L.; Li, Y. Structures, Mobility and Electronic Properties of Point Defects in Arsenene, Antimonene and an Antimony Arsenide Alloy. *J. Mater. Chem. C* **2017**, *5*, 4159−4166.

(10) Wang, G.; Pandey, R.; Karna, S. P. Atomically Thin Group V Elemental Films: Theoretical Investigations of Antimonene Allotropes. *ACS Appl. Mater. Interfaces* **2015**, *7*, 11490−11496.

DOI: 10.1021/acsami.7b08513
ACS Appl. Mater. Interfaces XXXX, XXX, XXX−XXX

(11) Aktürk, O. Ü.; Özçelik, V. O.; Ciraci, S. Single-layer Crystalline Phases of Antimony: Antimonenes. *Phys. Rev. B: Condens. Matter Mater. Phys.* **2015**, *91*, 235446.
(12) Kou, L.; Ma, Y.; Tan, X.; Frauenheim, T.; Du, A.; Smith, S. Structural and Electronic Properties of Layered Arsenic and Antimony Arsenide. *J. Phys. Chem. C* **2015**, *119*, 6918−6922.
(13) Chen, X. P.; Wang, L. M.; Sun, X.; Meng, R. S.; Xiao, J.; Ye, H. Y.; Zhang, G. Q. Sulfur Dioxide and Nitrogen Dioxide Gas Sensor Based on Arsenene: a First-principle Study. *IEEE Electron Device Lett.* **2017**, *38*, 661.
(14) Song, Z.; Liu, C.-C.; Yang, J.; Han, J.; Ye, M.; Fu, B.; Yang, Y.; Niu, Q.; Lu, J.; Yao, Y. Quantum Spin Hall Insulators and Quantum Valley Hall Insulators of BiX/SbX (X = H, F, Cl and Br) Monolayers with a Record Bulk Band Gap. *NPG Asia Mater.* **2014**, *6*, e147.
(15) Tsai, H.-S.; Wang, S.-W.; Hsiao, C.-H.; Chen, C.-W.; Ouyang, H.; Chueh, Y.-L.; Kuo, H.-C.; Liang, J.-H. Direct Synthesis and Practical Bandgap Estimation of Multilayer Arsenene Nanoribbons. *Chem. Mater.* **2016**, *28*, 425−429.
(16) Ares, P.; Aguilar-Galindo, F.; Rodríguez-San-Miguel, D.; Aldave, D. A.; Díaz-Tendero, S.; Alcamí, M.; Martín, F.; Gómez-Herrero, J.; Zamora, F. Mechanical Isolation of Highly Stable Antimonene under Ambient Conditions. *Adv. Mater.* **2016**, *28*, 6332−6336.
(17) Gibaja, C.; Rodriguez-San-Miguel, D.; Ares, P.; Gómez-Herrero, J.; Varela, M.; Gillen, R.; Maultzsch, J.; Hauke, F.; Hirsch, A.; Abellán, G.; Zamora, F. Few-layer Antimonene by Liquid-phase Exfoliation. *Angew. Chem., Int. Ed.* **2016**, *55*, 14470.
(18) Ji, J.; Song, X.; Liu, J.; Yan, Z.; Huo, C.; Zhang, S.; Su, M.; Liao, L.; Wang, W.; Ni, Z.; Hao, Y.; Zeng, H. Two-Dimensional Monocrystalline Antimoene Layers Grown by Van der Waals Epitaxy. *Nat. Commun.* **2016**, *7*, 13352.
(19) Huo, C.; Sun, X.; Yan, Z.; Song, X.; Liu, J.; Zhang, S.; Ji, J.; Jiang, L.; Xie, Z.; Zhou, S.; Zeng, H. Ultrathin Few-layer Antimonene: Large Yield Synthesis, Exact Atomical Structure and Outstanding Optical Limiting. *J. Am. Chem. Soc.* **2017**, *139*, 3568.
(20) Wu, X.; Shao, Y.; Liu, H.; Feng, Z.; Wang, Y.-L.; Sun, J.-T.; Liu, C.; Wang, J.-O.; Liu, Z.-L.; Zhu, S.-Y.; Wang, Y.-Q.; Du, S.-X.; Shi, Y.-G.; Ibrahim, K.; Gao, H.-J. Epitaxial Growth and Air-stability of Monolayer Antimonene on $PdTe_2$. *Adv. Mater.* **2017**, *29*, 1605407.
(21) Fortin-Deschênes, M.; Waller, O.; Menteş, T. O.; Locatelli, A.; Mukherjee, S.; Genuzio, F.; Levesque, P. L.; Hébert, A.; Martel, R.; Moutanabbir, O. Synthesis of Antimonene on Germanium. *Nano Lett.* **2017**, *17*, 4970.
(22) Lu, L.; Tang, X.; Cao, R.; Wu, L.; Li, Z.; Jing, G.; Dong, B.; Lu, S.; Li, Y.; Xiang, Y.; Li, J.; Fan, D.; Zhang, H. Broadband Nonlinear Optical Response in Few-Layer Antimonene and Antimonene Quantum Dots: A Promising Optical Kerr Media with Enhanced Stability. *Adv. Opt. Mater.* **2017**, 1700301.
(23) Tsai, H.-S.; Chen, C.-W.; Hsiao, C.-H.; Ouyang, H.; Liang, J.-H. The Advent of Multilayer Antimonene Nanoribbons with Room Temperature Orange Light Emission. *Chem. Commun.* **2016**, *52*, 8409−8412.
(24) Tran, V.; Yang, L. Scaling Laws for the Band Gap and Optical Response of Phosphorene Nanoribbons. *Phys. Rev. B: Condens. Matter Mater. Phys.* **2014**, *89*, 245407.
(25) Wang, X.; Jones, A. M.; Seyler, K. L.; Tran, V.; Jia, Y.; Zhao, H.; Wang, H.; Yang, L.; Xu, X.; Xia, F. Highly Anisotropic and Robust Excitons in Monolayer Black Phosphorus. *Nat. Nanotechnol.* **2015**, *10*, 517−521.
(26) Krasnozhon, D.; Lembke, D.; Nyffeler, C.; Leblebici, Y.; Kis, A. MoS_2 Transistors Operating at Gigahertz Frequencies. *Nano Lett.* **2014**, *14*, 5905−5911.
(27) Zhang, W.; Chiu, M.-H.; Chen, C.-H.; Chen, W.; Li, L.-J.; Wee, A. T. S. Role of Metal Contacts in High-Performance Phototransistors Based on WSe_2 Monolayers. *ACS Nano* **2014**, *8*, 8653−8661.
(28) Lopez-Sanchez, O.; Lembke, D.; Kayci, M.; Radenovic, A.; Kis, A. Ultrasensitive Photodetectors Based on Monolayer MoS_2. *Nat. Nanotechnol.* **2013**, *8*, 497−501.
(29) Liu, Y.; Weiss, N. O.; Duan, X.; Cheng, H.-C.; Huang, Y.; Duan, X. Van der Waals Heterostructures and Devices. *Nat. Rev. Mater.* **2016**, *1*, 16042.
(30) Allain, A.; Kang, J.; Banerjee, K.; Kis, A. Electrical Contacts to Two-dimensional Semiconductors. *Nat. Mater.* **2015**, *14*, 1195−1205.
(31) Schwierz, F.; Pezoldt, J.; Granzner, R. Two-dimensional Materials and their Prospects in Transistor Electronics. *Nanoscale* **2015**, *7*, 8261−8283.
(32) Leonard, F.; Talin, A. A. Electrical Contacts to One- and Two-dimensional Nanomaterials. *Nat. Nanotechnol.* **2011**, *6*, 773−783.
(33) Sun, Z.; Chang, H. Graphene and Graphene-like Two-Dimensional Materials in Photodetection: Mechanisms and Methodology. *ACS Nano* **2014**, *8*, 4133−4156.
(34) Lee, E. J. H.; Balasubramanian, K.; Weitz, R. T.; Burghard, M.; Kern, K. Contact and Edge Effects in Graphene Devices. *Nat. Nanotechnol.* **2008**, *3*, 486−490.
(35) Xia, F.; Mueller, T.; Golizadeh-Mojarad, R.; Freitag, M.; Lin, Y.-m.; Tsang, J.; Perebeinos, V.; Avouris, P. Photocurrent Imaging and Efficient Photon Detection in a Graphene Transistor. *Nano Lett.* **2009**, *9*, 1039−1044.
(36) Mueller, T.; Xia, F.; Freitag, M.; Tsang, J.; Avouris, P. Role of Contacts in Graphene Transistors: A Scanning Photocurrent Study. *Phys. Rev. B: Condens. Matter Mater. Phys.* **2009**, *79*, 245430.
(37) Park, J.; Ahn, Y. H.; Ruiz-Vargas, C. Imaging of Photocurrent Generation and Collection in Single-Layer Graphene. *Nano Lett.* **2009**, *9*, 1742−1746.
(38) Fontana, M.; Deppe, T.; Boyd, A. K.; Rinzan, M.; Liu, A. Y.; Paranjape, M.; Barbara, P. Electron-hole Transport and Photovoltaic Effect in Gated MoS_2 Schottky Junctions. *Sci. Rep.* **2013**, *3*, 1634.
(39) Zhang, Y.; Li, H.; Wang, L.; Wang, H.; Xie, X.; Zhang, S.-L.; Liu, R.; Qiu, Z.-J. Photothermoelectric and Photovoltaic Effects both Present in MoS_2. *Sci. Rep.* **2015**, *5*, 7938.
(40) Zhang, W.; Huang, J.-K.; Chen, C.-H.; Chang, Y.-H.; Cheng, Y.-J.; Li, L.-J. High-Gain Phototransistors Based on a CVD MoS_2 Monolayer. *Adv. Mater.* **2013**, *25*, 3456−3461.
(41) Yin, Z.; Li, H.; Li, H.; Jiang, L.; Shi, Y.; Sun, Y.; Lu, G.; Zhang, Q.; Chen, X.; Zhang, H. Single-Layer MoS_2 Phototransistors. *ACS Nano* **2012**, *6*, 74−80.
(42) Cui, X.; Lee, G.-H.; Kim, Y. D.; Arefe, G.; Huang, P. Y.; Lee, C.-H.; Chenet, D. A.; Zhang, X.; Wang, L.; Ye, F.; Pizzocchero, F.; Jessen, B. S.; Watanabe, K.; Taniguchi, T.; Muller, D. A.; Low, T.; Kim, P.; Hone, J. Multi-terminal Transport Measurements of MoS_2 Using a van der Waals Heterostructure Device Platform. *Nat. Nanotechnol.* **2015**, *10*, 534−540.
(43) Bandurin, D. A.; Tyurnina, A. V.; Yu, G. L.; Mishchenko, A.; Zólyomi, V.; Morozov, S. V.; Kumar, R. K.; Gorbachev, R. V.; Kudrynskyi, Z. R.; Pezzini, S.; Kovalyuk, Z. D.; Zeitler, U.; Novoselov, K. S.; Patanè, A.; Eaves, L.; Grigorieva, I. V.; Fal'ko, V. I.; Geim, A. K.; Cao, Y. High Electron Mobility, Quantum Hall Effect and Anomalous Optical Response in Atomically Thin InSe. *Nat. Nanotechnol.* **2016**, *12*, 223−227.
(44) Liu, Y.; Wu, H.; Cheng, H.-C.; Yang, S.; Zhu, E.; He, Q.; Ding, M.; Li, D.; Guo, J.; Weiss, N. O.; Huang, Y.; Duan, X. Toward Barrier Free Contact to Molybdenum Disulfide Using Graphene Electrodes. *Nano Lett.* **2015**, *15*, 3030−3034.
(45) Liu, Y.; Xiao, H.; Goddard, W. A. Schottky-Barrier-Free Contacts with Two-Dimensional Semiconductors by Surface-Engineered MXenes. *J. Am. Chem. Soc.* **2016**, *138*, 15853−15856.
(46) Kappera, R.; Voiry, D.; Yalcin, S. E.; Branch, B.; Gupta, G.; Mohite, A. D.; Chhowalla, M. Phase-Engineered Low-resistance Contacts for Ultrathin MoS_2 Transistors. *Nat. Mater.* **2014**, *13*, 1128−1134.
(47) Cho, S.; Kim, S.; Kim, J. H.; Zhao, J.; Seok, J.; Keum, D. H.; Baik, J.; Choe, D.-H.; Chang, K. J.; Suenaga, K.; Kim, S. W.; Lee, Y. H.; Yang, H. Phase Patterning for Ohmic Homojunction Contact in $MoTe_2$. *Science* **2015**, *349*, 625−628.
(48) Du, Y.; Yang, L.; Zhang, J.; Liu, H.; Majumdar, K.; Kirsch, P. D.; Ye, P. D. MoS_2 Field-effect Transistors with Graphene/Metal Heterocontacts. *IEEE Electron Device Lett.* **2014**, *35*, 599−601.

DOI: 10.1021/acsami.7b08513
ACS Appl. Mater. Interfaces XXXX, XXX, XXX−XXX

(49) Leong, W. S.; Luo, X.; Li, Y.; Khoo, K. H.; Quek, S. Y.; Thong, J. T. L. Low Resistance Metal Contacts to MoS_2 Devices with Nickel-Etched-Graphene Electrodes. *ACS Nano* **2015**, *9*, 869−877.
(50) Su, J.; Feng, L.; Zeng, W.; Liu, Z. Designing High Performance Metal-mMoS_2 Interfaces by Two-dimensional Insertions with Suitable Thickness. *Phys. Chem. Chem. Phys.* **2016**, *18*, 31092−31100.
(51) Kang, J.; Liu, W.; Sarkar, D.; Jena, D.; Banerjee, K. Computational Study of Metal Contacts to Monolayer Transition-Metal Dichalcogenide Semiconductors. *Phys. Rev. X* **2014**, *4*, 031005.
(52) Zhong, H.; Ni, Z.; Wang, Y.; Ye, M.; Song, Z.; Pan, Y.; Quhe, R.; Yang, J.; Yang, L.; Shi, J.; Lu, J. Interfacial Properties of Monolayer and Bilayer MoS_2 Contacts with Metals: Depressed Many-electron Effects. *Sci. Rep.* **2016**, *6*, 21786.
(53) Pan, Y.; Wang, Y.; Wang, L.; Zhong, H.; Quhe, R.; Ni, Z.; Ye, M.; Mei, W.-N.; Shi, J.; Guo, W.; Yang, J.; Lu, J. Graphdiyne-metal Contacts and Graphdiyne Transistors. *Nanoscale* **2015**, *7*, 2116−2127.
(54) Zheng, J.; Wang, Y.; Wang, L.; Quhe, R.; Ni, Z.; Mei, W.-N.; Gao, Z.; Yu, D.; Shi, J.; Lu, J. Interfacial Properties of Bilayer and Trilayer Graphene on Metal Substrates. *Sci. Rep.* **2013**, *3*, 2081.
(55) Pan, Y.; Wang, Y.; Ye, M.; Quhe, R.; Zhong, H.; Song, Z.; Peng, X.; Li, J.; Yang, J.; Shi, J.; Lu, J. Monolayer Phosphorene-Metal Interfaces. *Chem. Mater.* **2016**, *28*, 2100−2109.
(56) Pan, Y.; Li, S.; Ye, M.; Quhe, R.; Song, Z.; Wang, Y.; Zheng, J.; Pan, F.; Guo, W.; Yang, J.; Lu, J. Interfacial Properties of Monolayer $MoSe_2$−Metal Contacts. *J. Phys. Chem. C* **2016**, *120*, 13063−13070.
(57) Wang, Y.; Yang, R. X.; Quhe, R.; Zhong, H.; Cong, L.; Ye, M.; Ni, Z.; Song, Z.; Yang, J.; Shi, J.; Li, J.; Lu, J. Does p-type Ohmic Contact Exist in WSe_2-metal Interfaces? *Nanoscale* **2016**, *8*, 1179−1191.
(58) Blochl, P. E. Projector Augmented-wave Method. *Phys. Rev. B: Condens. Matter Mater. Phys.* **1994**, *50*, 17953−17979.
(59) Kresse, G.; Joubert, D. From Ultrasoft Pseudopotentials to the Projector Augmented-wave Method. *Phys. Rev. B: Condens. Matter Mater. Phys.* **1999**, *59*, 1758−1775.
(60) Kresse, G.; Hafner, J. Ab Initio Molecular-dynamics For Liquid-metals. *Phys. Rev. B: Condens. Matter Mater. Phys.* **1993**, *47*, 558−561.
(61) Kresse, G.; Hafner, J. Ab-initio Molecular-dynamics Simulation of the Liquid-metal Amorphous-semiconductor Transition in Germaniun. *Phys. Rev. B: Condens. Matter Mater. Phys.* **1994**, *49*, 14251−14269.
(62) Kresse, G.; Furthmuller, J. Efficiency of Ab-initio Total Energy Calculations for Metals and Semiconductors Using a Plane-wave Basis Set. *Comput. Mater. Sci.* **1996**, *6*, 15−50.
(63) Kresse, G.; Furthmuller, J. Efficient Iterative Schemes for Ab Initio Total-energy Calculations Using a Plane-wave Basis Set. *Phys. Rev. B: Condens. Matter Mater. Phys.* **1996**, *54*, 11169−11186.
(64) Monkhorst, H. J.; Pack, J. D. Special Points for Brillouin-zone Integrations. *Phys. Rev. B* **1976**, *13*, 5188−5192.
(65) *Atomistix ToolKit*; QuantumWise A/S, Copenhagen, Denmark, 2016.
(66) Das, S.; Zhang, W.; Demarteau, M.; Hoffmann, A.; Dubey, M.; Roelofs, A. Tunable Transport Gap in Phosphorene. *Nano Lett.* **2014**, *14*, 5733−5739.
(67) Qiao, J.; Kong, X.; Hu, Z.-X.; Yang, F.; Ji, W. High-mobility Transport Anisotropy and Linear Dichroism in Few-layer Black Phosphorus. *Nat. Commun.* **2014**, *5*, 4475.
(68) Tran, V.; Soklaski, R.; Liang, Y.; Yang, L. Layer-controlled Band Gap and Anisotropic Excitons in Few-layer Black Phosphorus. *Phys. Rev. B: Condens. Matter Mater. Phys.* **2014**, *89*, 235319.
(69) Cai, Y.; Zhang, G.; Zhang, Y.-W. Layer-dependent Band Alignment and Work Function of Few-layer Phosphorene. *Sci. Rep.* **2015**, *4*, 6677.
(70) Du, Y.; Liu, H.; Deng, Y.; Ye, P. D. Device Perspective for Black Phosphorus Field-Effect Transistors: Contact Resistance, Ambipolar Behavior, and Scaling. *ACS Nano* **2014**, *8*, 10035−10042.
(71) Giovannetti, G.; Khomyakov, P. A.; Brocks, G.; Karpan, V. M.; van den Brink, J.; Kelly, P. J. Doping Graphene with Metal Contacts. *Phys. Rev. Lett.* **2008**, *101*, 026803.
(72) Guo, Y.; Pan, F.; Ye, M.; Wang, Y.; Pan, Y.; Zhang, X.; Li, J.; Zhang, H.; Lu, J. Interfacial Properties of Stanene−metal Contacts. *2D Mater.* **2016**, *3*, 035020.
(73) Guo, Y.; Pan, F.; Ye, M.; Sun, X.; Wang, Y.; Li, J.; Zhang, X.; Zhang, H.; Pan, Y.; Song, Z.; Yang, J.; Lu, J. Monolayer Bismuthene-Metal Contacts: a Theoretical Study. *ACS Appl. Mater. Interfaces* **2017**, *9*, 23128−23140.
(74) Wang, Y.; Li, J.; Xiong, J.; Pan, Y.; Ye, M.; Guo, Y.; Zhang, H.; Quhe, R.; Lu, J. Does the Dirac Cone of Germanene Exist on Metal Substrates? *Phys. Chem. Chem. Phys.* **2016**, *18*, 19451−19456.
(75) Quhe, R.; Yuan, Y.; Zheng, J.; Wang, Y.; Ni, Z.; Shi, J.; Yu, D.; Yang, J.; Lu, J. Does the Dirac Cone Exist in Silicene on Metal Substrates? *Sci. Rep.* **2015**, *4*, 5476.
(76) Kim, C.; Moon, I.; Lee, D.; Choi, M. S.; Ahmed, F.; Nam, S.; Cho, Y.; Shin, H.-J.; Park, S.; Yoo, W. J. Fermi Level Pinning at Electrical Metal Contacts of Monolayer Molybdenum Dichalcogenides. *ACS Nano* **2017**, *11*, 1588−1596.
(77) Shih, C.-J.; Wang, Q. H.; Son, Y.; Jin, Z.; Blankschtein, D.; Strano, M. S. Tuning On−Off Current Ratio and Field-Effect Mobility in a MoS_2−Graphene Heterostructure via Schottky Barrier Modulation. *ACS Nano* **2014**, *8*, 5790−5798.
(78) Boča, R.; Hajko, P.; Benco, L.; Benkovský, I.; Faktor, D. Thin Layers of Grey Arsenic: A Molecular Orbital Study. *Czech. J. Phys.* **1993**, *43*, 813−819.
(79) McDonnell, S.; Addou, R.; Buie, C.; Wallace, R. M.; Hinkle, C. L. Defect-Dominated Doping and Contact Resistance in MoS_2. *ACS Nano* **2014**, *8*, 2880−2888.
(80) Schwierz, F. Graphene Transistors. *Nat. Nanotechnol.* **2010**, *5*, 487−496.
(81) Quhe, R.; Zheng, J.; Luo, G.; Liu, Q.; Qin, R.; Zhou, J.; Yu, D.; Nagase, S.; Mei, W.-N.; Gao, Z.; Lu, J. Tunable and Sizable Band Gap of Single-layer Graphene Sandwiched between Hexagonal Boron Nitride. *NPG Asia Mater.* **2012**, *4*, e6.

DOI: 10.1021/acsami.7b08513
ACS Appl. Mater. Interfaces XXXX, XXX, XXX−XXX